Nanoscale

PAPER

View Article Online
View Journal | View Issue

Cite this: *Nanoscale*, 2025, **17**, 15829

Impact of solvent and ligand density on the self-assembly and optical properties of metal nanocrystals†

Alessandro Cangiano,[a,b] Noemi Gallucci,[a,b] Antonella Giarra, [a] Junaid Ali,[a,b] Leonardo Chiappisi,[c] Nathan P. Cowieson[d] and Luigi Paduano *[a,b]

Metal nanocrystals (M-NCs) and their supramolecular assemblies have attracted significant interest from the scientific community due to their wide range of applications arising from the possibility of accurately tuning the M-NCs properties through self-assembly into supramolecular aggregates. In this study, we investigate the complex interplay between capping agent surface coverage and solvent-capping agent interactions in the self-assembly process of M-NCs into supramolecular structures. Specifically, we explore the self-assembly behavior of gold (Au-NCs), silver (Ag-NCs), and platinum (Pt-NCs) nanocrystals upon functionalization with oleic acid (OA) in water using a microemulsion approach. Through a multi-technique analysis, we demonstrate the critical role of ligand density and solvent choice in driving the formation of highly ordered supramolecular structures. By increasing the surface coverage of the M-NC ligands, we observed a transition to more organised assemblies, with the interaction between the oleylamine alkyl chain and the functionalization medium further modulating the type of supramolecular arrangement. Moreover, we highlight the profound influence of both the external environment and supramolecular aggregation on the optical properties of the M-NCs. This work provides crucial insights into the factors that govern nanocrystals' self-assembly and optical behavior, with broad implications for the design and application of nanomaterials in nanotechnology and materials science.

Received 16th April 2025,
Accepted 10th June 2025

DOI: 10.1039/d5nr01560j

rsc.li/nanoscale

Introduction

Metal nanocrystals (M-NCs), such as those of gold (Au), silver (Ag), and platinum (Pt),[1,2] have garnered particular attention due to their peculiar properties that have paved the way for their use in several fields including sensing, energy conversion, and medical diagnostics, highlighting the growing importance of M-NCs in addressing both scientific challenges and industrial needs.[3–7]

These nanostructures are characterised by a high specific surface area and a significant number of surface atoms, which collectively impart a broad spectrum of unique and valuable properties, including enhanced catalytic activity, tunable optical behaviours, and improved electronic characteristics.[8,9]

Various methodologies have been explored to optimize the properties and functionality of these NCs. One of the most widespread strategies involves the careful design and synthesis of M-NCs with tailored shapes and sizes.[10,11] Researchers have devoted considerable effort to understanding how geometric factors, such as shape, size, and the influence of the ligand on these structural aspects, influence the physico-chemical properties of M-NCs. These structural features also determine how the NCs interact with the environment, which in turn impacts their overall performance.[12,13]

Additionally, an emerging strategy for tailoring the physico-chemical properties of M-NCs involves the creation of three-dimensional nanoscale-ordered assemblies.[14]

These ordered systems offer a wealth of new possibilities, as the spatial arrangement and orientation of nanocrystals within a structured assembly can significantly influence their collective behaviour, particularly their plasmonic properties. The plasmonic band, a key feature of metal nanocrystals, can be altered and tuned by inducing specific ordered structures, such as face-centred cubic (FCC) or hexagonal close-packed (HCP) phases, which can result in enhanced or distinct optical and electronic behaviors.[15,16] This approach opens new avenues for the development of advanced materials with

[a]*Department of Chemical Sciences, University of Naples Federico II, 80126 Naples, Italy. E-mail: lpaduano@unina.it*
[b]*CSGI, Center for Colloid and Surface Science, 50019 Sesto Fiorentino, Italy*
[c]*LSS Group, Institut Laue-Langevin, 6 rue Jules Horowitz BP 156, Grenoble F-38042, Cedex 9, France*
[d]*Diamond Light Source, Didcot, Oxfordshire, England, UK*
† Electronic supplementary information (ESI) available. See DOI: https://doi.org/10.1039/d5nr01560j

custom-designed optical responses, which could be applied to areas such as sensing, imaging, and energy harvesting.

For this approach, understanding how the interaction between solvents,[17] capping agents,[18] and metal nanocrystals affect their aggregation and ordering is essential for the design of systems in which the nanocrystals can be organized into predictable and functional structures.[19,20] The density and type of coating agent can significantly impact the formation of nanocrystal aggregates, with potential effects on the optical and plasmonic properties of the material.[21,22]

In this study, we examined the physico-chemical properties of gold (Au-NCs), silver (Ag-NCs), and platinum (Pt-NCs) nanocrystals, each coated with oleylamine as a capping agent. Our primary objective was to explore how different organic solvents, specifically cyclohexane, toluene, ethyl ether, and chloroform, influence the optical properties and aggregation behaviour of these M-NCs. Additionally, we focused on how the ligand extension in the organic solvent and the ligand density on the NCs surface affect the spatial distribution and organisation of nanocrystals during the aggregation process, which was achieved using an emulsion method. This process involved transferring the nanocrystals into aqueous solutions through oleic acid (OA) coating, which facilitated the formation of nanocrystal supramolecular aggregates with distinct structural characteristics. The findings from this work offer valuable insights into the optimisation of M-NCs for various applications, providing a deeper understanding of how molecular interactions and assembly processes can be controlled to design materials with tailored properties.

Results and discussion

Parameters such as the surface capping density of metal nanocrystals and the nature of the solvent in which they are dispersed to form superlattice structures will be discussed in the following sections. These structures are, in fact, obtained through the emulsion method, which entails transferring the nanocrystals from an apolar solvent to an aqueous medium. The discussion will first focus on characterizing the chemical and physical properties of the synthesized NCs, particularly in relation to the polarity of the dispersing medium.

Influence of solvent dielectric constant and ligand density on the physico-chemical properties of nanocrystals

The oleylamine capping shells of gold (Au-NCs), silver (Ag-NCs), and platinum (Pt-NCs) nanocrystals were qualitatively and quantitatively characterised, given their crucial role in defining the physico-chemical properties of nanocrystals and their influence on the self-assembly process. FTIR analysis, presented in Fig. 1A, verified the successful formation of oleylamine (whose chemical structure is presented in Fig. 1C) capping shells on the surface of all the NCs.[23,24] The peaks located at about 2850 cm^{-1} and 2930 cm^{-1} correspond to the –C–H stretching of the capping agent carbon chain.[25] Notably, the intensity of these peaks decreased systematically from Au-NCs to Ag-NCs and further to Pt-NCs, suggesting a reduced quantity of oleylamine on the surfaces of the NCs. These results were confirmed by TGA analysis as shown in Fig. 1B. Oleylamine coating decomposition occurred at higher temperatures and over a broader range of temperatures than free oleylamine, implying the formation of strong bonds between the capping agent and the NCs surfaces.[26,27] Moreover, the ligand density on the NC surfaces was determined using the formula in eqn (3) (see Materials and method section), yielding values of 4.0 ± 0.2 chains per nm^2 (~94% surface coverage) for Au-NCs, 2.8 ± 0.5 chains per nm^2 (~70% surface coverage) for Ag-NCs, and 1.4 ± 0.4 chains per nm^2 (~35% surface coverage) for Pt-NCs, respectively. These results confirm that Au-NCs exhibit the highest ligand density, followed by Ag-NCs, while Pt-NCs show the lowest coverage.

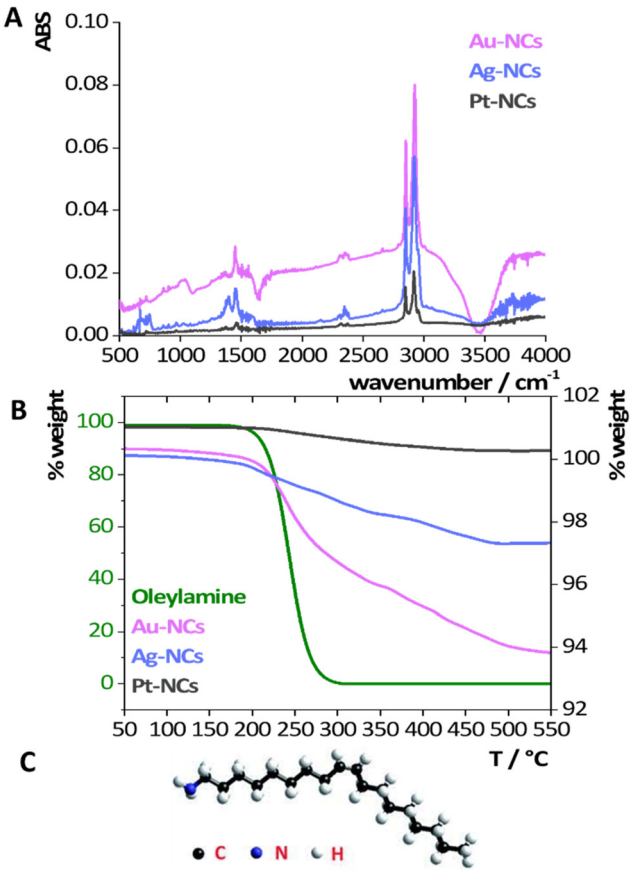

Fig. 1 FTIR Spectra of oleylamine-coated Au-NCs (pink line), Ag-NCs (blue line), and Pt-NCs (black line) (A), TGA curve of free oleylamine (green line) and oleylamine-coated Au-NCs (pink line), Ag-NCs (blue line), and Pt-NCs (black line). Left *y*-axis is for free oleylamine, and right *y*-axis is for oleylamine-coated M-NCs (B), oleylamine ($CH_3(CH2)7CH{=}CH(CH2)8NH2$) chemical structure (C).

These findings confirm that the amino group exhibits low affinity for the surface of Pt nanocrystals, while showing a stronger affinity for gold surfaces compared to silver surfaces.[28–31]

Despite variation in ligand density among the M-NCs, the synthetic protocols employed yielded spherical NCs, as illus-

trated by the TEM images reported in Fig. S1.† Statistical analysis of several TEM images revealed a mean radius of 4.5 ± 0.8 nm for Au-NCs, 4.0 ± 0.9 nm for Ag-NCs, and 4.4 ± 0.8 nm for Pt-NCs.

The external environment's effect on the physico-chemical properties of the M-NCs was investigated by varying the nature of the solvent in which the M-NCs were dispersed. Particularly, four solvents were selected: cyclohexane, toluene, ethyl ether, and chloroform, whose properties are detailed in Table S1.†

DLS data in Fig. 2 indicate a decrease in the hydrodynamic radius of individual NCs as the solvent's dielectric constant increases from 2.02 C^2 (N m^2)$^{-1}$ for cyclohexane to 4.81 C^2 (N m^2)$^{-1}$ for chloroform.

The experimental evidence revealed that the smallest hydrodynamic radius was observed in the case of NCs dissolved in chloroform. Moreover, the DLS data shows a bimodal distribution of hydrodynamic radius for Ag-NCs and Pt-NCs when dispersed in chloroform. Particularly, the second observed population is centred at 30 nm and 180 nm for Ag-NCs and Pt-NCs respectively, pointing out the tendency for these two M-NCs species to aggregate when dispersed in chloroform. This is related to two main aspects. First, the Ag-NCs and Pt-NCs have a lower ligand density compared to Au-NCs. Second, in chloroform, the oleylamine alkyl chain adopts a less extended conformation, which diminishes the steric stabilisation of the M-NCs.

In general, the comparison of the hydrodynamic radii and the average size of the inorganic nuclei obtained from TEM analysis to which is added a length of about 2.5 nm of the oleylamine chain (calculated using the Tanford equation[32]), a systematic decrease of the alkyl chains is observed as the dielectric constant of the solvent increases.

This correlation between the hydrodynamic radius and the solvent dielectric constant can be understood in terms of solvent–ligand interactions. In low dielectric constant solvents, favourable interactions promote an extended conformation of the oleylamine alkyl chain, maximizing its steric barrier to aggregation. In contrast, in solvents with higher dielectric constant, the diminished solvation of the hydrophobic chain induces a more compact conformation that minimizes solvent exposure.[33]

Moreover, the propensity for aggregation observed in Ag-NCs and Pt-NCs dispersed in chloroform is closely related to their lower ligand density. Insufficient surface coverage reduces steric repulsion, allowing attractive van der Waals interactions to predominate, which leads to enhanced aggregation of these nanocrystals.[34]

In addition to aggregation behavior, the medium in which they are dispersed also has a huge impact on the optical properties of these systems.[35,36]

The UV-Vis spectra reported in Fig. S2† show that the absorption maxima position (λ_{max}) of oleylamine-coated M-NCs is influenced by changes in the surrounding media, particularly the solvent's refractive index across all systems.

Notably, we observed a red shift in λ_{max} as the refractive index increased, with an 8 nm shift for Au-NCs, 14 nm for Ag-NCs, and 30 nm for Pt-NCs (see Table S2† for λ_{max} values for all systems). In general, such a shift can be attributed to various factors, including NCs' shape and size, the nature of the amphiphilic coating, and the refractive index of the surrounding medium.[37]

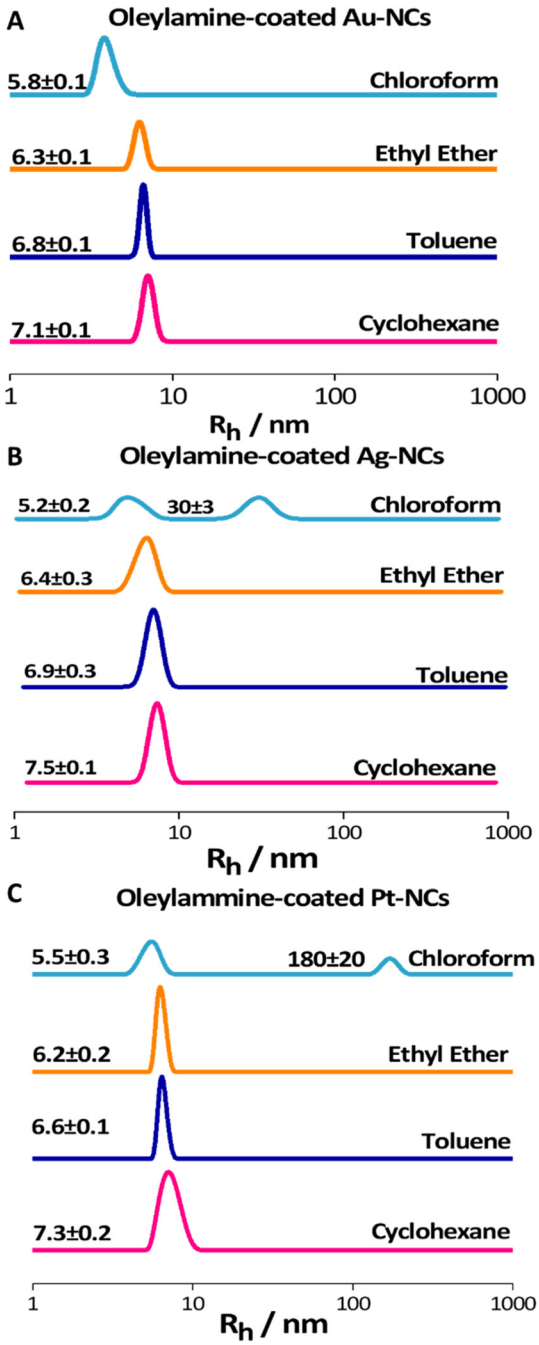

Fig. 2 Hydrodynamic radii distribution of oleylamine-coated Au NCs (A), oleylamine-coated Ag-NCs (B), and oleylamine-coated Pt-NCs (C) dispersed in increasing dielectric constant solvents: in cyclohexane, toluene, ethyl ether, and chloroform.

In our study, we ruled out any effect of size, shape, and coating because we utilize particles of approximately the same size, which are monodisperse and have a spherical shape and

the same coating. Our analysis showed that the shift of λ_{max} was influenced by the medium, particularly the refractive index of the solvent, which alters the local electromagnetic field of the NCs based on the medium's density and polarization.[38,39]

A clear and effective way to analyze the impact of solvent nature on the optical properties of NCs is through a comparative study of refractive index sensitivity. The refractive index sensitivity, S, is defined as:

$$S = \frac{d\lambda_{max}}{dn} \quad (1)$$

where λ_{max} represents the max of the localized surface plasmon resonance (LSPR) wavelength, and n denotes the refractive index of the dielectric environment surrounding the metal NCs. The unit of refractive index sensitivity is nm per RIU, where RIU stands for refractive index unit.[40–42]

We derived S by plotting λ_{max} as a function of the refractive index of the solvent and performing a linear fit of the experimental data points (Fig. 3).

S, the slope of this fit, characterizes the variation in λ_{max} per unit change in the refractive index.[43,44]

A higher S value indicates greater sensitivity to changes in the refractive index. As illustrated in Fig. 3, Pt-NCs exhibit the highest sensitivity to changes in the refractive index (S = 214 nm per RIU), while Au-NCs display the least sensitivity (S = 54 nm per RIU).

Our measured refractive index sensitivity values align with previous theoretical predictions for gold and silver nanocrystals within the 20–80 nm size range. Specifically, our results confirm that silver NCs demonstrate higher sensitivity than their gold counterparts and that sensitivity decreases with smaller NC dimensions.[45] For instance, M. Hamamoto *et al.*[42] reported a refractive index sensitivity of 33 nm per RIU for 9 nm Au-NCs, which closely matches the values observed in our study (about 2.5 nm of radius). This agreement not only validates our experimental approach but also highlights the potential significance of the NCs presented herein.

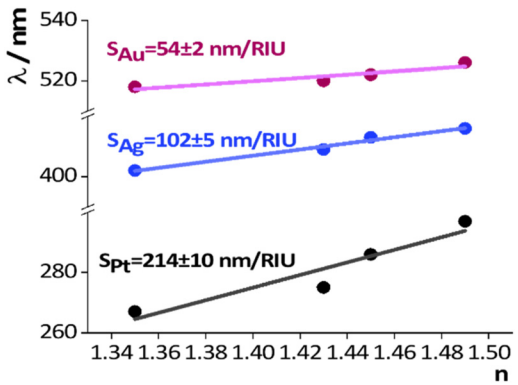

Fig. 3 λ_{max} as a function of the solvent refractive index, and the linear fit to determine the sensitivity. Au-NCs (pink), Ag-NCs (blue), and Pt-NCs (Black).

Experimental evidence clearly shows that the stability of individual NCs is closely linked to their ability to form a dense molecular layer, covering at least 70% of the surface in this case, which prevents disordered aggregation (as will be discussed below). Furthermore, the solvent in which the hybrid nanocrystals are dispersed prior to their assembly into a superlattice plays a crucial role in this process.

Factors that affect the self-assembly of individual nanocrystals into supramolecular ordered aggregates

The self-assembly of NCs into supramolecular aggregates is a complex process influenced by multiple factors, primarily the dielectric constant of the dispersing solvent, which influences the configuration and extension of the oleylamine alkyl chain, and the ligand density on the NC surfaces.[46–48]

To provide a clear understanding of these interdependencies, we present the results by sorting the NCs based on their ligand density. This systematic approach allows for a detailed exploration of how solvent properties interact with surface chemistry to influence self-assembly outcomes.

Influence of solvent dielectric constant on high ligand density NCs self-assembly: Au-NCs

As seen in the previous sections, Au-NCs have a higher ligand density than Ag-NCs and Pt-NCs. This was also the only system that could be functionalised in water, with OA from all the organic solvents being the only monodisperse system in all of them. The dispersion of Au-NCs in cyclohexane and toluene promotes in both cases a C14 Frank–Kasper phase organisation within the supramolecular aggregate in water (Fig. 4 and 5).

SAXS analysis revealed a characteristic Q/Q_1 ratio (Table S3†). Notably, in Fig. 4B, the presence of three prepeaks further confirms this arrangement, as there are key features of C14 Frank–Kasper (C14 FK) phases.[49,50] These findings are strongly corroborated by high-resolution imaging tech-

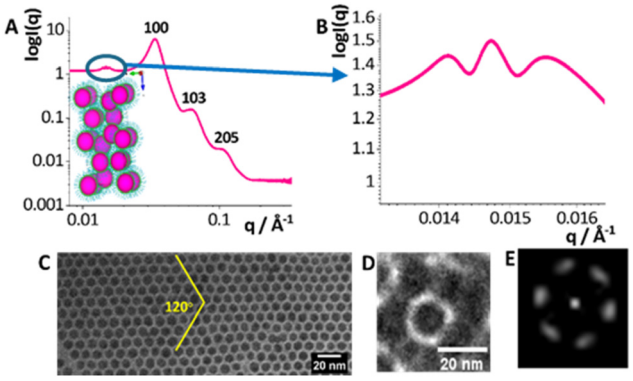

Fig. 4 SAXS pattern for OA@Au-NCs in water from cyclohexane, and 3D schematic representation of the supramolecular C14 Frank–Kasper arrangement (A), enlarged view of the scattering profile presented in (A), emphasizing the three characteristic peaks that identify the Frank–Kasper phase.(B), cryo-EM image for OA@Au-NCs from cyclohexane, scale bar 20 nm (C), cryo-EM image for OA@Au-NCs from cyclohexane, scale bar 20 nm (D), FTT obtained on the (D) area (E).

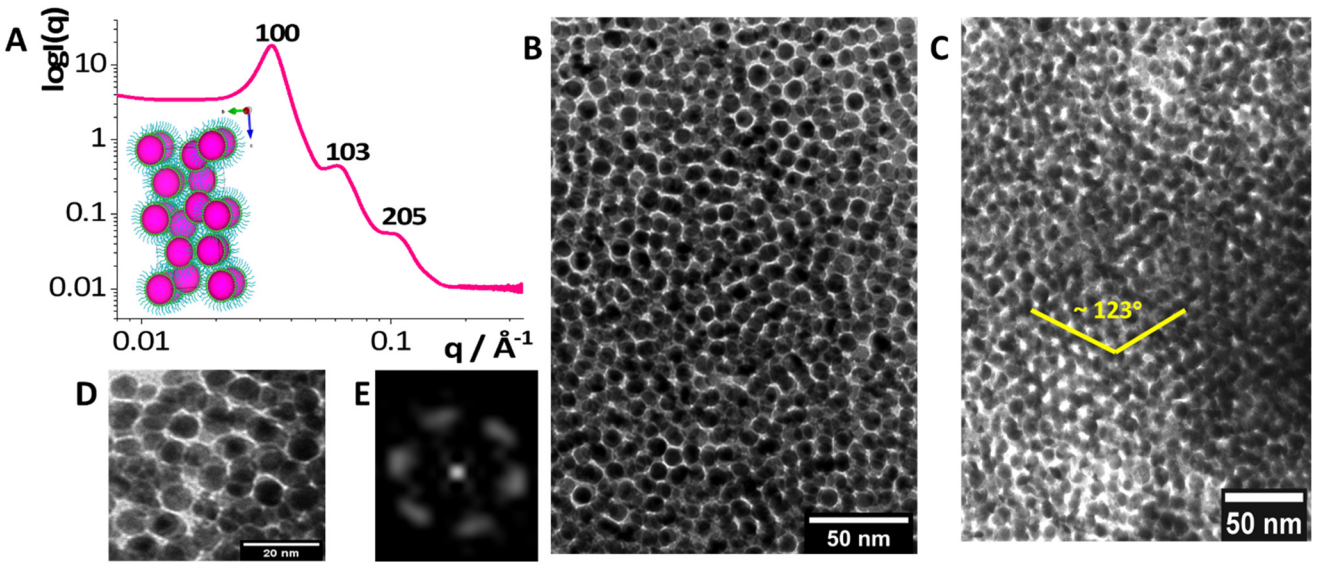

Fig. 5 SAXS pattern for OA@Au-NCs in water from toluene, and 3D schematic representation of the supramolecular C14 FK arrangement (A), TEM image for OA@Au-NCs from toluene, scale bar 50 nm (B), TEM image for OA@Au-NCs from toluene, scale bar 50 nm (C), TEM image for OA@Au-NCs from toluene, scale bar 20 nm (D) FTT obtained on the (D) area (E).

niques. Cryo-EM images of OA@Au-NCs dispersed in cyclohexane (Fig. 4C–E) and TEM images of OA@Au-NCs dispersed in toluene (Fig. 5B–E) show the characteristic honeycomb-like structure, where 12 neighbouring NCs surround one central nanocrystal. Additionally, angular alignments of ~120° between NC rows were observed, consistent with the expected geometry of C14 FK arrangements.[49,51]

Supramolecular aggregates obtained from a solvent with a higher dielectric constant, such as ethyl ether, in which the alkyl chain of oleylamine is not fully extended, resulted in the formation of a different organization within the supramolecular aggregate in water, as shown in Fig. 6. In particular, due to the consideration of ~90° angle between the NC rows and characteristic peak ratios, Q/Q_1 (Table S4†), of the SAXS, it was possible to identify an FCC phase of the aggregate in water. When it comes to chloroform, Au-NCs do not exhibit order within the supramolecular aggregate, as shown in Fig. S3.†

A rigorous quantitative analysis of the SAXS data from the ordered supramolecular assemblies enabled the precise determination of the unit cell parameters, which are comprehensively summarized in Table 1.

The analytical relationships employed in this derivation are detailed in the Materials and methods section.

The results presented in this section show that increasing the dielectric constant of the organic solvent in which the NCs are dispersed, and the consequent modifications of the oleylamine alkyl chain interactions with the solvent has a strong influence on the type of structuring observed in the supramolecular aggregate upon functionalization in water with OA, arriving to the point where carrying out the functionalization in water of Au-NCs in chloroform the particles are less inclined to arrange themselves in ordered supramolecular aggregates.

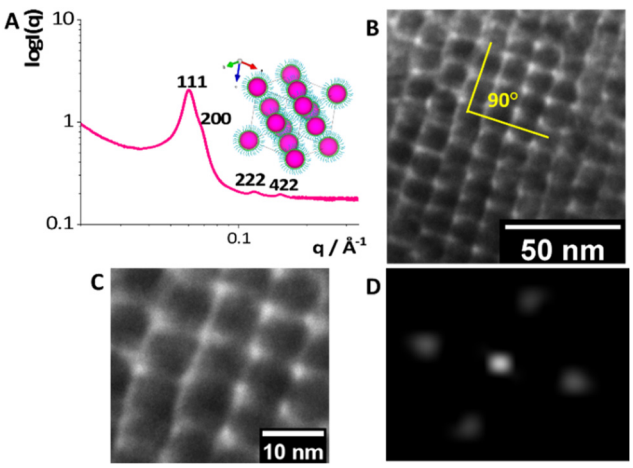

Fig. 6 SAXS pattern for OA@Au-NCs in water from ethyl ether, and 3D schematic representation of the FCC supramolecular structure (A), TEM image for OA@Au-NCs, scale bar 50 nm (B), TEM image for OA@Au-NCs, scale bar 10 nm (C), FTT obtained on the (C) area (D).

Influence of solvent dielectric constant on intermediate ligand density NCs self-assembly: Ag-NCs

Ag-NCs present an intermediate degree of coverage compared to the other M-NCs under analysis in the present study. Upon functionalization with OA in water, we observed that the results varied a lot from one solvent to another. Supramolecular aggregates in water, obtained from the functionalization of Ag-NCs dispersed in cyclohexane, exhibit features of a C14 Frank–Kasper organization (Fig. 7). The SAXS Q/Q_1 in Table S3† and the angular alignment of ~123° between the NC rows corroborate this arrangement. This is further confirmed by the presence of the

Table 1 SAXS derived unit cell parameters. *d*: smallest distance between neighbouring NCs, *e*: minimum thickness of the ligand shell

System	Order	*a*/nm	*b*/nm	*c*/nm	*d*/nm	*e*/nm
OA@Au-NCs from cyclohexane		21.5	21.5	35.1	10.7	1.7
OA@Au-NCs from Toluene		21.7	21.7	35.4	10.8	1.8
OA@Au-NCs from Ethyl ether		19.1	19.1	19.1	13.5	4.5

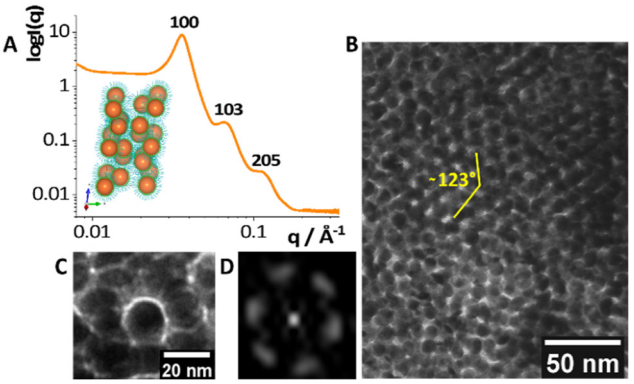

Fig. 7 SAXS pattern for OA@Ag-NCs in water from cyclohexane, and 3D schematic representation of the C14 Frank–Kasper supramolecular structure (A), TEM image for OA@Ag-NCs, scale bar 50 nm (B), TEM image for OA@Ag-NCs, scale bar 20 nm (C), FTT obtained on the (C) area (D).

typical honeycomb structure, where one central NC is surrounded by 12 NCs.

By applying the equations reported in the Materials and methods section and considering the OA@Au-NCs C14 Frank–Kasper phases, we also determined, in this case, the lattice parameters that were $a = b = 20.0$ nm, $c = 32.7$ nm, $d = 10.0$ nm, and $e = 2.0$ nm.

On the other hand, clusters of OA@Ag-NCs in water obtained from Ag-NCs dispersed in toluene and diethyl ether (Fig. 8) did not show any typical features of an ordered supramolecular aggregate. However, for both samples, SAXS measurements allowed the determination of a typical interparticle pattern distance of ~10 nm.

These results indicate that a reduced ligand density on the surface of M-NCs hinders their ability to self-assemble into ordered supramolecular structures, especially when an

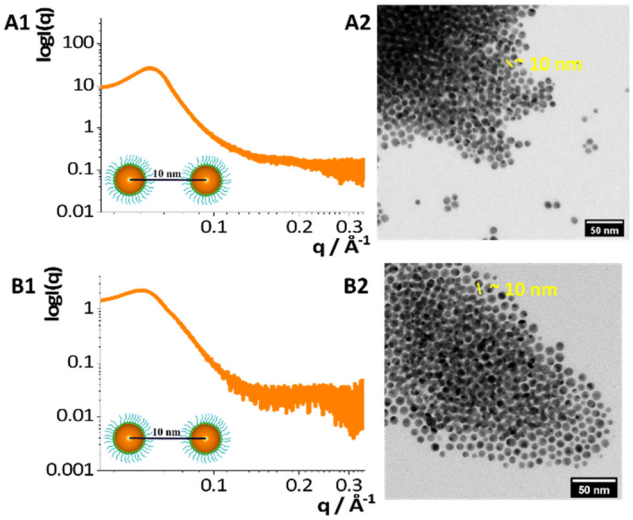

Fig. 8 SAXS pattern for OA@Ag-NCs in water obtained from toluene, and schematic representation of the core-core distance between the NCs (A1), TEM image for OA@Ag-NCs from toluene, scale bar 50 nm (A2), SAXS pattern for OA@Ag-NCs in water obtained from ethyl ether, and schematic representation of the core–core distance between the NCs (B1), TEM image for OA@Ag-NCs from ethyl ether, scale bar 50 nm (B2).

increase in the dielectric constant of the dispersing solvent alters the conformation of the oleylamine alkyl chains due to less favorable solvent–chain interactions.

Influence of solvent dielectric constant on low ligand density NCs self-assembly: Pt-NCs

The results of the Pt-NCs functionalization from all three solvents, presented in Fig. 9, highlighted the formation of disordered aggregates. This lack of organization is attributed to the comparatively lower ligand density on Pt-NCs surface (~35% surface coverage), reducing interparticle interactions necessary for ordered self-assembly.

For the OA@Pt-NCs in water obtained from both cyclohexane and toluene, SAXS curves (Fig. 9A1 and B2) were successfully fitted using the model described in eqn (10) (see Materials and methods section), or both samples, the low-q region was characterised by a power-law decay of q^{-3}, characteristic of mass fractal aggregates.

At higher-q values, the core–shell sphere model allowed us to fit the curve and obtain structural parameters. For OA@Pt-NCs in water obtained from cyclohexane, we obtained a core radius = 4.3 ± 0.5 nm and a shell thickness = 2.5 ± 0.1 nm, and for OA@Pt-NCs in water obtained from toluene, we obtained a core radius = 4.6 ± 0.5 nm and a shell thickness = 2.0 ± 0.1 nm. These results align with the Pt-NC core size derived from the statistical analysis of the TEM images and the oleylamine chain length estimated *via* the Tanford equation.

In the case of OA@Pt-NCs obtained from ethyl ether (Fig. 9C1 and C2), we have the formation of a disordered aggregate. In this case, it was only possible to determine the SAXS

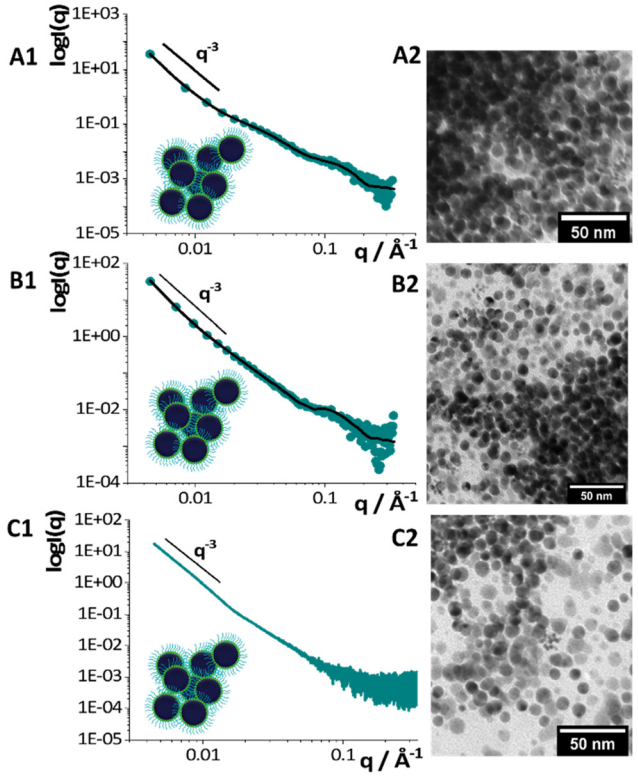

Fig. 9 SAXS pattern for OA@Pt-NCs in water from cyclohexane (A1), TEM image for OA@Pt-NCs from cyclohexane, scale bar 50 nm (A2) SAXS pattern for OA@Pt-NCs in water from toluene (B1), TEM image for OA@Pt-NCs from toluene, scale bar 50 nm (B2), SAXS pattern for OA@Pt-NCs in water from ethyl ether (C1), TEM image for OA@Pt-NCs from ethyl ether, scale bar 50 nm (C2). In all cases, the functionalisation of Pt-NCs leads to the formation of disordered supramolecular structures, independently from the dispersing solvent, as illustrated in the 3D schematic representations in the SAXS panel.

intensity decrease as a function of q as a q^{-3} power law, typical of a mass fractal.

Supramolecular aggregates' optical properties

An interesting aspect of these systems is their optical properties, particularly the effect that the nature of the structuring within the supramolecular structure has on them.[52–54]

Our investigation of the optical properties of OA@M-NCs in water yielded significant results. First, the reported spectra in Fig. 10 shows, significant differences in the spectra profile with respect to the individual M-NCs in organic solvents. This is linked to the fact that the localized surface plasmon resonance (LSPR) of M-NCs is strongly influenced by the presence of other M-NCs in their vicinity.[55] For instance in an FCC structure, the minimum distance between two neighboring the minimum distance between two neighbouring nanocrystals is greater rather than in a C14 FK structure, as determined for the OA@Au-NCs system in the structural characterisation section.

These findings underscore the intricate relationship between the structural configuration and optical properties of M-NCs, which is crucial for the fine design of nanomaterials with specific properties.

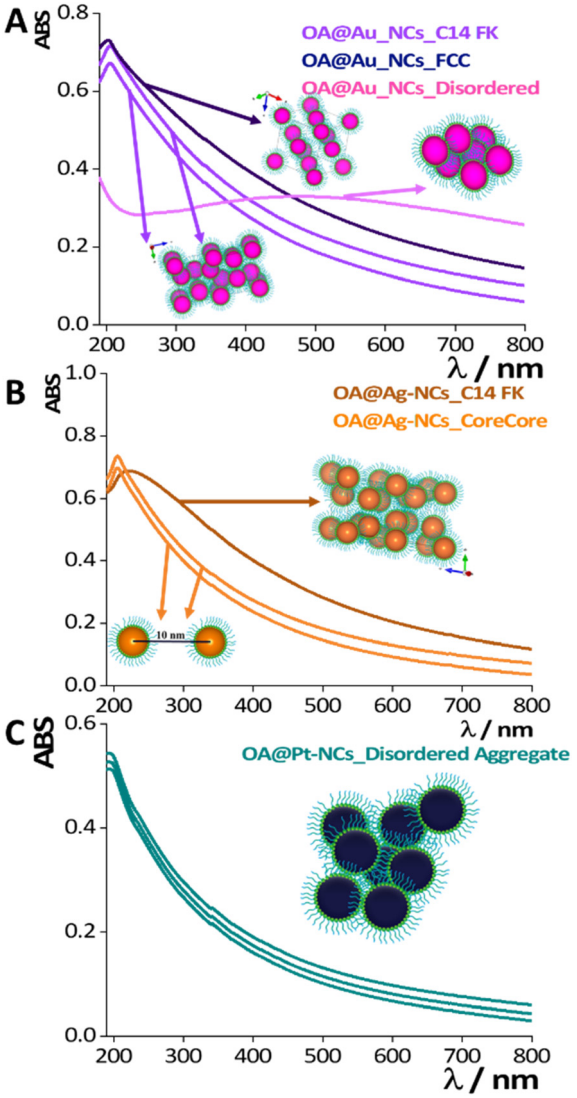

Fig. 10 UV-Vis Spectra for OA@Au-NCs includes, in violet, the UV-Vis absorption spectrum of the FCC ordered assembly (with a 3D schematic representation); in light violet, the absorption spectrum of the C14 FK phases assemblies, which, independently of the functionalization solvent, give rise to the same absorption properties (with a 3D schematic representation); and in magenta, the UV-Vis spectra for the disordered assembly of OA@Au-NCs with its 3D schematic representation (A). The UV-Vis Spectra for OA@Ag-NCs shows, in dark orange, the absorption spectrum of the C14 FK phase assembly (with a 3D schematic representation) and in orange, the UV-Vis spectra for the repetitive core–core distance assembly of OA@Ag-NCs with its 3D schematic representation (B). Lastly, the UV-Vis spectra for the OA@Pt-NCs disordered assembly and their schematic 3D representation highlight the formation of a disordered aggregate in all cases, which resulted in the same optical properties, independently of the functionalization solvent (C).

Tuning order: how solvent polarity and ligand density shape nanocrystal self-assembly

Understanding the combined influence of the solvent's dielectric constant and the ligand density on the surface of NCs is crucial for modulating their self-assembly into supramolecular structures. In the previous sections, we highlighted how vari-

ations in these parameters govern the spatial organization and packing efficiency of NCs, ultimately dictating whether ordered aggregates can form.

Moreover, understanding how these parameters can be leveraged to modulate the formation of specific ordered aggregates is crucial for the rational design of structures with tailored optical properties, as discussed in the previous section.

The results illustrated in this study showed that higher ligand density enhances steric stabilization and facilitates the formation of ordered aggregates. In our study, we proved that Au-NCs exhibit the highest ligand density, enabling robust packing and consistent ordering across various solvent conditions. In contrast, Ag-NCs, with intermediate ligand density, form ordered aggregates in low-polarity solvents but struggle to achieve similar organization in polar environments. Pt-NCs, characterized by the lowest ligand density, fail to establish ordered arrangements under most conditions, as reduced steric repulsion leads to aggregation dominated by van der Waals interactions.[56]

The study of all systems reveals a profound interdependence between the dielectric constant of the dispersing solvent and the ligand density on the NC surface, collectively governing supramolecular organization. The dispersing solvent primarily dictates the spatial conformation and flexibility of the ligand shells, modulating interparticle interactions and assembly dynamics. Conversely, ligand density exerts a decisive influence on steric stabilization, dictating the NCs' ability to resist attractive forces and achieve ordered packing. These insights underscore the necessity of a dual-parameter optimization strategy, balancing solvent properties with surface chemistry, to precisely control self-assembly processes.

To better elucidate the influence of the oleylamine ligand shell on the self-assembly of M-NCs into ordered supramolecular structures, we calculated the e/L ratio, where e is the minimum thickness of the ligand shell, and L is the oleylamine carbon chain length. This parameter is crucial in understanding how the ligand shell characteristics influence the self-assembly into ordered supramolecular structures.

In the case of the OA@Au-NCs exhibiting FCC organization, the calculated e/L was 1.8, which denotes little to no interpenetration of the ligand chain. This finding is consistent with the predictions of the Optimal Packing Model (OPM), which describes close-packing arrangements without significant ligand interdigitation.[57–59] The FCC organization was observed when the supramolecular aggregate in water was obtained from the functionalization of Au-NCs dispersed in ethyl ether, where it was found that the oleylamine alkyl chain was in a different conformation, due to the less favourable interaction with the solvent, which inhibited interdigitation during the self-assembly process.

In the case of the C14 FK supramolecular structures, we obtained an e/L equal to 0.7, 0.75, and 0.8 for OA@Au-NCs obtained from cyclohexane, OA@Au-NCs obtained from toluene, and OA@Ag-NCs obtained from cyclohexane, respectively. These values are consistent with the Overlapping Cone Model (OCM), which describes a densely interdigitated ligand shell arrangement.[57–59]

Interestingly, a solvent-dependent increase in e/L was observed within the C14 FK structures. For Au-NCs C14 FK assemblies, the higher ratio obtained in OA@Au-NCs in water obtained from the functionalization of Au-NCs dispersed in toluene, compared to the OA@Au-NCs in water obtained from the functionalization of Au-NCs in cyclohexane, is due to the conformational changes of oleylamine alkyl chain in toluene, which prevents optimal packing. This variation underscores the interplay between ligand flexibility and solvent interactions in modulating structural organization. Additionally, the observed differences in packing efficiency between Au-NCs and Ag-NCs are attributed to the lower ligand coverage on Ag-NCs. Reduced ligand density on Ag-NCs limits steric stabilization and introduces structural heterogeneity, affecting the overall supramolecular arrangement.

The e/L ratio values reported in this study are consistent with findings by Pansu *et al.*[49] where alkane-thiol-capped Au-NCs exhibited hexagonal packing when $e/L < 1$, while FCC arrangements were observed for e/L values between 1.0 and 1.8. This agreement reinforces the validity of the observed trends and highlights the utility of the e/L ratio as a predictive metric for supramolecular assembly behavior across different capping ligands and solvent conditions.

Conclusions

In summary, this study thoroughly explored the impact of solvents with increasing dielectric constant and different refractive index, such as ethyl ether, chloroform, cyclohexane, and toluene, on the properties of coated metal nanocrystals. The difference in refractive index differentially affects the optical properties of synthesized NCs. Specifically, our results confirm that silver NCs demonstrate higher sensitivity than their gold counterparts and that sensitivity decreases with smaller NC dimensions.

We also investigated how the dialectic constant of the dispersing medium (solvent polarity) and the degree of surface coating of alkyl molecules, which is strongly influenced by the interaction of the amine group with respect to the metal,[60,61] can influence the formation of ordered supramolecular aggregates, including FCC and C14 FK phases. Our comprehensive approach revealed that metal nanocrystals with high ligand density can form different ordered supramolecular structures, and that the type of structure can be modulated by varying the dielectric constant of the dispersing solvent. These findings highlight the importance of the ligand alkyl chain conformation in the self-assembly. The obtained results underscore the importance of optimizing both the solvent environment and surface chemistry to control the structural assembly of M-NCs.

Materials and methods

Materials

Gold(III) chloride solution (99.99% trace metal basis, 30 wt% in dilute HCl), silver nitrate ($AgNO_3$) (>99.0%), platinum acetyl-

acetonate (97%) ($Pt(C_5H_7O_2)_2$), oleylamine (technical grade 70%), chloroform (>99.5% contains 100–200 ppm amylenes as a stabilizer), toluene (>99.7%), ethyl ether (>99.8% contains BHT as inhibitor), cyclohexane (>99.5), acetone, ethanol 96% were purchased from Merck (Germany) and used without further purification. All aqueous solutions were prepared using double-distilled Milli-Q water and filtered using 0.20 μm filters.

All the NC syntheses were conducted in such a way as to have the same nanocrystal precursor and oleylamine ratio (equal to 0.01).

Au-NCs synthesis

50 μL of HCl solution of $HAuCl_4$ and 1.5 mL of oleylamine were added in a 25 mL three-neck flask. First, the mixture was heated up to 60 °C for 10 minutes to allow the homogenization of the reaction mixture, then it was heated to 140 °C and kept at this temperature for 30 minutes, at the end of which it was heated up to 230 °C and kept in this condition for 60 minutes.[62] The whole process was carried out under Argon atmosphere to prevent the occurrence of unwanted secondary reactions. At the end of the synthesis, 10 mL of ethanol was added to the mixture and centrifugated for 10 minutes at 8000 rpm; the procedure was repeated three times to wash out all the unreacted starting reagents. The final product was stored in cyclohexane, toluene, ethyl ether, or chloroform.

Ag-NCs synthesis

0.1013 g of $AgNO_3$ and 20 mL of oleylamine were added in a three-neck 100 mL flask. The reaction mixture was heated up to 60 °C for 10 minutes to favour the homogenization of the reaction mixture, then it was heated up to 190 °C and kept at this temperature for 60 minutes.[63] The whole process was carried out under an inert Argon atmosphere to prevent the occurrence of secondary unwanted reactions. At the end of the synthesis 40 mL of acetone was added to the mixture and centrifugated for 10 minutes at 8000 rpm; the procedure was repeated three times. The final product was stored in cyclohexane, toluene, ethyl ether, or chloroform.

Pt-NCs synthesis

0.02 g of Platinum acetylacetonate and 5 mL of oleylamine were added to a 25 mL three-neck flask. First, the reaction mixture was heated up to 80 °C for 15 minutes to favour the homogenization of the reaction mixture, and then it was heated up to 190 °C for 60 minutes.[64] The system was kept under argon atmosphere for the whole process to prevent the occurrence of unwanted secondary reactions. At the end of the process 10 mL of ethanol was added to the mixture and centrifugated for 10 minutes at 8000 rpm; this step was repeated three times. The final product was stored in cyclohexane, toluene, ethyl ether, or chloroform.

Nanocrystals functionalization

The NCs were functionalized using a microemulsion functionalization approach, where the oleic acid (OA) was used as a functionalization agent. A certain amount of Au, Ag, or Pt-NCs was placed in a glass vial and then a specific amount of OA was added to the NCs and well mixed in such a way to have a 10 : 1 (NCs : OA) molar ratio. Particularly, in the present work we used 1 mM M-NCs suspensions and a stock solution of 1 mM OA. OA was added to the organic suspension of M-NCs since it is not well soluble in water. At this point, water was added driving the formation of a biphasic system. Such sample was then tip sonicated for 5 minutes to allow the formation of a monophasic system, and after that, the samples were left under magnetic stirring for 24 hours to allow the evaporation of the organic solvent.[65]

Dynamic light scattering (DLS)

Dynamic Light Scattering (DLS) experiments were carried out to determine the sizes of the supposed monodispersity and the effect of the solvent on the hydrodynamic radius of the NCs here obtained. The measurements were carried out employing an LSI spectrometer composed of a fibre-coupled laser operating at 638 nm. The experiments were recorded at a constant temperature of (25.0 ± 0.1) °C using a thermostatic bath, with a scattering angle θ of 90°.

The experiments were carried out for each system on at least 3 independent samples. The correlation functions were analyzed with the CORENN algorithm, and the obtained diffusion coefficient was used to estimate the hydrodynamic radius, R_h, using the Stokes–Einstein equation:

$$R_h = \frac{kT}{6\pi\eta_0\langle D\rangle} \quad (2)$$

where k is the Boltzman constant, T is the absolute temperature, and η_0 is the solvent viscosity. This allowed us to obtain the hydrodynamic radius of the scattering object.[66,67]

Transmission electron microscopy (TEM)

Morphology and core dimensions of the NCs were studied by Transmission Electron Microscopy (TEM) using a FEI TECNAI G2 200 kV microscope (FEI Company, Dawson Creek Drive Hillsboro, OR, USA). The samples were prepared by placing 5 μL of a given sample onto a carbon-coated grid and allowed to air dry before imaging. All the acquired images were analysed using the ImageJ software.[68]

Cryo-EM sample preparation and data collection

For Cryo-EM experiments, sample vitrification was carried out using a Mark IV Vitrobot (Thermo Fisher Scientific). 3 μL of OA@Au-NCs suspension was placed on a C-Flat 1.2/1.3-300 Cu grid previously glow discharged at 30 mA for 30 s in a GloQube (Quorum Technologies). The sample was blotted and plunge-frozen into liquid ethane. The vitrified sample was transferred to a Talos Artica transmission electron microscope (Thermo Fisher Scientific) and EPU 2.8 (Thermo Fisher Scientific) software. All acquired images were analysed using ImageJ software.

Fourier transform infrared spectroscopy (FTIR)

Fourier-transform Infrared Spectroscopy was employed to evaluate the capping agent surface coverage of the NCs. The experiments were carried out using an FTIR 4700LE (Jasco Europe Srl, Lecco, Italy) in the range 400–4000 cm^{-1}. Spectra were recorded in ATR mode by accumulating 128 scans with a resolution of 2 cm^{-1}. Particularly, to be able to compare the results obtained from this analysis to get a relative coating degree of the M-NCs we prepared Au-NCs, Ag-NCs, and Pt-NCs suspension at the same concentration of 1 mM, and then the same amount of such suspensions (100 μL) were transferred onto a KBr pellet, let dry and then analysed.

UV-visible spectroscopy

UV-visible spectroscopy measurements were performed using a Jasco V-750 instrument (Jasco Europe Srl, Lecco, Italy) equipped with a deuterium lamp (190–350 nm) and a halogen lamp (330–900 nm) to study the absorption properties of the here studied NCs. The experiments were performed using a quartz cuvette with an optical path of 1 cm, using a bandwidth of 1 nm and a scanning speed of 200 nm min^{-1}.

Thermogravimetric analysis (TGA)

TGA analyses were conducted using a PerkinElmer Pyris Diamond TG/DT Analyser. A sample of approximately 20 mg was analysed in the temperature range of 50 °C to 550 °C at a 10 °C per minute under nitrogen flow.

Ligand density was calculated applying the following equation:

$$\sigma = \frac{\frac{wt\%_{shell}}{wt\%_{core}}\rho_{core}\frac{4}{3}\pi {r_{core}}^3 N_A}{M_w 4\pi {r_{core}}^2} \quad (3)$$

where N_A is the Avogadro number, ρ_{core} is core bulk density, r_{core} is M-NCs core radius, and M_w is the oleylamine molecular weight.[69]

Small angle X-ray scattering (SAXS)

The ordered structuring of the functionalized NCs was investigated by Small Angle X-ray Scattering (SAXS) experiments. Such experiments were conducted at the Diamond Light Source B21 beamline (Didcot, United Kingdom). B21 beamline configuration consisted of a beam energy of 13.018 keV and a sample-to-detector distance of 3.7 m. With this setup, we collected data for the scattering vector modulus $Q = 4\pi \sin(\theta/2)\lambda$ between 0.0045 $Å^{-1}$ and 0.34 $Å^{-1}$, where θ is the scattering angle.[70]

C14 FK phase unit cell parameters were derived using the following equations:

$$a = \frac{2}{\sqrt{3}}\frac{2\pi}{q_{100}} \quad (4)$$

$$c = \sqrt{\frac{8}{3}}a \quad (5)$$

$$d = \frac{a}{2} \quad (6)$$

$$e = 2r_{core} - d \quad (7)$$

FCC unit cell parameters were derived as:

$$a = \sqrt{3}\frac{2\pi}{q_{111}} \quad (8)$$

$$d = \frac{a}{\sqrt{2}} \quad (9)$$

OA@Pt-NCs data were analysed using the appropriate model to fit the data. In the present work, experimental data were fitted with the SASView v5.0.6 Software (**https://www.sasview.org/**) using a plugin model that combines the Power Law and the Core–Shell Sphere models.

$$I(q) = \text{scale} \cdot q^{-\text{power}} + \frac{\text{scale}}{V}F^2(q) + \text{background} \quad (10)$$

where

$$F(q) = \frac{3}{V_s}\left[V_c(\rho_c - \rho_s)\frac{\sin(qr_c) - qr_c\cos(qr_c)}{(qr_c)^3}\right] + \left[V_s(\rho_s - \rho_{solv})\frac{\sin(qr_s) - qr_s\cos(qr_s)}{(qr_s)^3}\right] \quad (11)$$

where V_s is the volume of the whole particle, V_c is the core volume, r_s = radius + thickness is the radius of the particle, r_c is the core radius, ρ_c is the core scattering length density, ρ_s is the shell scattering density, ρ_{shell} is the solvent scattering length density.[71]

Author contributions

A. C. data curation, formal analysis, methodology, investigation, visualization, and writing the original draft. N. G. conceptualization, data curation, investigation, methodology, writing – reviewing and editing. A. G. formal analysis. J. A. formal analysis. L. C. resources. N. P. C. validation and resources. L. P. conceptualization, funding acquisition, project administration, resources, supervision, writing – reviewing, and editing.

Conflicts of interest

There are no conflicts to declare.

Data availability

The data supporting this article have been included in the manuscript and as part of the ESI.† The raw data is available from the corresponding author upon reasonable request.

Acknowledgements

A. C., N. G., and L. P. wish to thank Diamond Light Source for providing beamtime (Reference SM30763-4). We kindly acknowledge the University of Milan Unitech NOLIMITS Center for granting access to the cryo-EM facility. The authors also thank the ILL for the use of support facilities within the Partnership for Soft Condensed Matter.

The project is financed by the National Recovery and Resilience Plan (NRRP) funded by the European Union – NextGenerationEU, Cascade Call Project "Nanoprobes for the retinal diagnosis of neurodegenerative diseases (NANOEYE)", funded under the Tuscany Health Ecosystem (ECS_00000017), CUP: E67G24000380006.

References

1 F. Montanarella and M. V. Kovalenko, *ACS Nano*, 2022, **16**(4), 5085–5102.
2 E. C. Garnett, B. Ehrler, A. Polman and E. Alarcon-Llado, *ACS Photonics*, 2021, **8**, 61–70.
3 N. Gallucci, A. Cangiano, S. Russo, G. Pota, R. D. Girolamo, E. Martinez, N. Vaxelaire, L. Paduano and G. Vitiello, *Mater. Chem. Front.*, 2024, **8**, 3973–3984.
4 V. Venezia, M. Verrillo, N. Gallucci, R. Di Girolamo, G. Luciani, G. D'Errico, L. Paduano, A. Piccolo and G. Vitiello, *J. Environ. Chem. Eng.*, 2023, **11**, 108973.
5 Q. N. Nguyen, C. Wang, Y. Shang, A. Janssen and Y. Xia, *Chem. Rev.*, 2023, **123**, 3693–3760.
6 W. Wang, M. Zhang, Z. Pan, G. M. Biesold, S. Liang, H. Rao, Z. Lin and X. Zhong, *Chem. Rev.*, 2022, **122**, 4091–4162.
7 C. Li, N. Clament Sagaya Selvam and J. Fang, *Nano-Micro Lett.*, 2023, **15**, 83.
8 N. Joudeh and D. Linke, *J. Nanobiotechnol.*, 2022, **20**, 262.
9 S. D. Marchi, S. Núñez-Sánchez, G. Bodelón, J. Pérez-Juste and I. Pastoriza-Santos, *Nanoscale*, 2020, **12**, 23424–23443.
10 Y. Shi, Z. Lyu, M. Zhao, R. Chen, Q. N. Nguyen and Y. Xia, *Chem. Rev.*, 2021, **121**, 649–735.
11 L. Wang, M. Hasanzadeh Kafshgari and M. Meunier, *Adv. Funct. Mater.*, 2020, **30**, 2005400.
12 A. Luchini, G. D'Errico, S. Leone, Z. Vaezi, A. Bortolotti, L. Stella, G. Vitiello and L. Paduano, *Colloids Surf., B*, 2018, **168**, 2–9.
13 A. Luchini, G. Vitiello, F. Rossi, O. R. D. Ballesteros, A. Radulescu, G. D'Errico, D. Montesarchio, C. de J. Fernández and L. Paduano, *Phys. Chem. Chem. Phys.*, 2015, **17**, 6087–6097.
14 F. Schulz, O. Pavelka, F. Lehmkühler, F. Westermeier, Y. Okamura, N. S. Mueller, S. Reich and H. Lange, *Nat. Commun.*, 2020, **11**, 3821.
15 X. Li, X. Liu and X. Liu, *Chem. Soc. Rev.*, 2021, **50**, 2074–2101.
16 M. B. Ross, J. C. Ku, V. M. Vaccarezza, G. C. Schatz and C. A. Mirkin, *Nat. Nanotechnol.*, 2015, **10**, 453–458.
17 L. L. Missoni and M. Tagliazucchi, *ACS Nano*, 2020, **14**, 5649–5658.
18 K. J. Si, Y. Chen, Q. Shi and W. Cheng, Nanoparticle Superlattices: The Roles of Soft Ligands – Si, *Adv. Sci.*, 2018, **5**, 1700179.
19 A. Luchini, R. K. Heenan, L. Paduano and G. Vitiello, Functionalized SPIONs: the surfactant nature modulates the self-assembly and cluster formation, *Phys. Chem. Chem. Phys.*, 2016, **18**, 18441–18449.
20 A. Luchini, Y. Gerelli, G. Fragneto, T. Nylander, G. K. Pálsson, M.-S. Appavou and L. Paduano, *Colloids Surf., B*, 2017, **151**, 76–87.
21 J. Choi and B. H. Kim, *Nanomaterials.*, 2024, **14**(20), 1685.
22 S. L. Westcott, S. J. Oldenburg, T. R. Lee, and N. J. Halas, Formation and Adsorption of Clusters of Gold Nanoparticles onto Functionalized Silica Nanoparticle Surfaces, *Langmuir*, 1998, **14**(19), 5396–5401.
23 M. Amir, A. Baykal, H. Sözeri, H. Gungunes and S. E. Shirsath, *Arabian J. Chem.*, 2019, **12**(8), 4971–4981.
24 M. Nagamine, M. Osial, J. Widera-Kalinowska, K. Jackowska and P. Krysiński, *Nanomaterials*, 2020, **10**, 2437.
25 S. Mourdikoudis and L. M. Liz-Marzán, Oleylamine in Nanoparticle Synthesis, *Chem. Mater.*, 2013, **25**(9), 1465–1476.
26 R. Borah, R. Ninakanti, G. Nuyts, H. Peeters, A. Pedrazo-Tardajos, S. Nuti, C. Vande Velde, K. De Wael, S. Lenaerts, S. Bals and S. W. Verbruggen, *Chem. – Eur. J.*, 2021, **27**, 9011–9021.
27 N. Karouta, Y. V. Simos, G. Basina, K. Spyrou, M. Subrati, A. V. Chatzikonstantinou, M. A. Hammami, V. Tzitzios, S. M. Alhassan, Y. Al Wahedi, A. P. Douvalis, G. C. Hadjipanayis, K. Tsamis, E. Dounousi, G. S. Markopoulos, S. Bellou, V. Georgakilas, D. Peschos, Z. Sideratou, H. Stamatis, D. P. Gournis and E. P. Giannelis, *ACS Appl. Nano Mater.*, 2023, **6**, 2770–2783.
28 J. Cure, Y. Coppel, T. Dammak, P. F. Fazzini, A. Mlayah, B. Chaudret and P. Fau, Monitoring the Coordination of Amine Ligands on Silver Nanoparticles Using NMR and SERS, *Langmuir*, 2015, **31**(4), 1362–1367.
29 Y. Lyu, L. M. Becerril, M. Vanzan, S. Corni, M. Cattelan, G. Granozzi, M. Frasconi, P. Rajak, P. Banerjee, R. Ciancio, F. Mancin and P. Scrimin, *Adv. Mater.*, 2024, **36**, 2211624.
30 S. Nath, S. K. Ghosh, S. Kundu, S. Praharaj, S. Panigrahi and T. Pal, *J. Nanopart. Res.*, 2006, **8**, 111–116.
31 A. H. Pakiari and Z. Jamshidi, *J. Phys. Chem. A*, 2007, **111**, 4391–4396.
32 A. Rahdar, H. Beyzaei, F. Askari and G. Z. Kyzas, *Appl. Phys. A*, 2020, **126**, 324.
33 S. Leekumjorn, S. Gullapalli and M. S. Wong, *J. Phys. Chem. B*, 2012, **116**, 13063–13070.
34 A. Sánchez-Iglesias, M. Grzelczak, T. Altantzis, B. Goris, J. Pérez-Juste, S. Bals, G. Van Tendeloo, S. H. Donaldson Jr., B. F. Chmelka, J. N. Israelachvili and L. M. Liz-Marzán, *ACS Nano*, 2012, **6**, 11059–11065.

35 O. Saison-Francioso, G. Lévêque, A. Akjouj, Y. Pennec, B. Djafari-Rouhani, S. Szunerits and R. Boukherroub, *J. Phys. Chem. C*, 2012, **116**, 17819–17827.
36 M. Habibi Masheli, S. Eyvazi, M. Aghdaee and J. M. Amjad, *J. Phys. Chem. C*, 2023, **127**, 23696–23705.
37 P. S. Popovetskiy, A. I. Bulavchenko, M. G. Demidova and T. Yu. Podlipskaya, *J. Struct. Chem.*, 2015, **56**, 357–364.
38 K. L. Kelly, E. Coronado, L. L. Zhao and G. C. Schatz, *J. Phys. Chem. B*, 2003, **107**, 668–677.
39 A. C. Templeton, J. J. Pietron, R. W. Murray and P. Mulvaney, *J. Phys. Chem. B*, 2000, **104**, 564–570.
40 A. Rabbani, R. Rudacille and K. Hasegawa, *J. Phys. Chem. C*, 2024, **128**, 19210–19221.
41 P. N. D. Prajna and R. K. Sinha, *Plasmonics*, 2025, **20**, 1351–1364.
42 M. Hamamoto and H. Yagyu, *J. Nanopart. Res.*, 2023, **25**, 158.
43 H. R. Hegde, S. Chidangil and R. K. Sinha, *J. Mater. Sci.: Mater. Electron.*, 2022, **33**, 4011–4024.
44 P. Tuersun, T. Yusufu, A. Yimiti and A. Sidike, *Optik*, 2017, **149**, 384–390.
45 J. Singh Sekhon and S. S. Verma, *Plasmonics*, 2011, **6**, 311–317.
46 E. Cepeda-Perez, D. Doblas, T. Kraus and N. de Jonge, *Sci. Adv.*, 2020, **6**, eaba1404.
47 C. L. Bassani, G. van Anders, U. Banin, D. Baranov, Q. Chen, M. Dijkstra, M. S. Dimitriyev, E. Efrati, J. Faraudo, O. Gang, N. Gaston, R. Golestanian, G. I. Guerrero-Garcia, M. Gruenwald, A. Haji-Akbari, M. Ibáñez, M. Karg, T. Kraus, B. Lee, R. C. Van Lehn, R. J. Macfarlane, B. M. Mognetti, A. Nikoubashman, S. Osat, O. V. Prezhdo, G. M. Rotskoff, L. Saiz, An-Chang Shi, S. Skrabalak, I. I. Smalyukh, M. Tagliazucchi, D. V. Talapin, A.i V. Tkachenko, S. Tretiak, D. Vaknin, A. Widmer-Cooper, G. C. L. Wong, X. Ye, S. Zhou, E. Rabani, M. Engel, and A. Travesset, Nanocrystal Assemblies: Current Advances and Open Problems, *ACS Nano*, 2024, **18**(23), 14791–14840.
48 Z.-P. Lv, M. Kapuscinski and L. Bergström, *Nat. Commun.*, 2019, **10**, 4228.
49 B. Pansu, C. Goldmann, D. Constantin, M. Impéror-Clerc and J.-F. Sadoc, *Soft Matter*, 2021, **17**, 6461–6469.
50 S. Hajiw, B. Pansu, and J. F. Sadoc, Evidence for a C14 Frank–Kasper Phase in One-Size Gold Nanoparticle Superlattices, *ACS Nano*, 2015, **9**(8), 8116–8121.
51 N. Gallucci, M.-S. Appavou, N. Cowieson, G. D'Errico, R. Di Girolamo, S. Lettieri, F. Sica, G. Vitiello and L. Paduano, *J. Colloid Interface Sci.*, 2024, **659**, 926–935.
52 J. Liu, H. He, D. Xiao, S. Yin, W. Ji, S. Jiang, D. Luo, B. Wang and Y. Liu, *Materials*, 2018, **11**, 1833.
53 A. T. M. Yeşilyurt and J.-S. Huang, *Adv. Opt. Mater.*, 2021, **9**, 2100848.
54 K. L. Young, M. B. Ross, M. G. Blaber, M. Rycenga, M. R. Jones, C. Zhang, A. J. Senesi, B. Lee, G. C. Schatz and C. A. Mirkin, *Adv. Mater.*, 2014, **26**, 653–659.
55 Y. Wang, Z. Yang and J. Wei, *J. Phys. Chem. C*, 2022, **126**, 4948–4958.
56 J. K. Stolarczyk, A. Deak and D. F. Brougham, Nanoparticle Clusters: Assembly and Control Over Internal Order, Current Capabilities, and Future Potential, *Adv. Mater.*, 2016, **28**, 5400–5424.
57 M. A. Boles, M. Engel and D. V. Talapin, *Chem. Rev.*, 2016, **116**, 11220–11289.
58 N. Olichwer, T. Koschine, A. Meyer, W. Egger, K. Rätzke and T. Vossmeyer, *RSC Adv.*, 2016, **6**, 113163–113172.
59 P. Schapotschnikow and T. J. H. Vlugt, *J. Chem. Phys.*, 2009, **131**, 124705.
60 G. Wang, C. Ma, L. Zheng and Y. Chen, *J. Mater. Chem. A*, 2021, **9**, 19534–19553.
61 H.-J. Yin, J.-H. Zhou and Y.-W. Zhang, *Inorg. Chem. Front.*, 2019, **6**, 2582–2618.
62 J. Choi, S. Park, Z. Stojanović, H.-S. Han, J. Lee, H. K. Seok, D. Uskoković and K. H. Lee, *Langmuir*, 2013, **29**, 15698–15703.
63 S. Peng, J. M. McMahon, G. C. Schatz, S. K. Gray and Y. Sun, *Proc. Natl. Acad. Sci. U. S. A.*, 2010, **107**, 14530–14534.
64 Z. Liu, E. Ada, W. Reichert and D. Nikles, *J. Power Sources*, 2007, **164**, 472–480.
65 N. Gallucci, G. Vitiello, R. Di Girolamo, P. Imbimbo, D. M. Monti, O. Tarallo, A. Vergara, I. Russo Krauss and L. Paduano, *Nanomaterials*, 2021, **11**, 542.
66 A. Accardo, D. Tesauro, G. Morelli, E. Gianolio, S. Aime, M. Vaccaro, G. Mangiapia, L. Paduano and K. Schillén, *J. Biol. Inorg. Chem.*, 2007, **12**, 267–276.
67 A. Accardo, R. Mansi, A. Morisco, G. Mangiapia, L. Paduano, D. Tesauro, A. Radulescu, M. Aurilio, L. Aloj, C. Arra and G. Morelli, *Mol. BioSyst.*, 2010, **6**, 878–887.
68 C. A. Schneider, W. S. Rasband and K. W. Eliceiri, *Nat. Methods*, 2012, **9**, 671–675.
69 B. V. Tawade, M. Singh, I. E. Apata, J. Veerasamy, N. Pradhan, A. Karim, J. F. Douglas and D. Raghavan, *JACS Au*, 2023, **3**, 1365–1375.
70 N. P. Cowieson, C. J. C. Edwards-Gayle, K. Inoue, N. S. Khunti, J. Doutch, E. Williams, S. Daniels, G. Preece, N. A. Krumpa, J. P. Sutter, M. D. Tully, N. J. Terrill and R. P. Rambo, *J. Synchrotron Radiat.*, 2020, **27**, 1438–1446.
71 S. A. Rice, *J. Polym. Sci.*, 1956, **19**, 594–594.